Front. Mater. Sci. 2023, 17(2): 230646
https://doi.org/10.1007/s11706-023-0646-8

RESEARCH ARTICLE

# Revealing component synergy of Ni–Fe/black phosphorous composites synthesized by self-designed electrochemical method for enhancing photoelectrocatalytic oxygen evolution reaction

He Xiao[1], Shoufeng Xue[1], Zimei Fu[1], Man Zhao (✉)[1], Li Zhang[1], Junming Zhang[1], Haishun Wu[1], Jianfeng Jia (✉)[1], and Nianjun Yang (✉)[2]

1 Key Laboratory of Magnetic Molecules & Magnetic Information Materials (Ministry of Education), School of Chemistry and Materials Science, Shanxi Normal University, Taiyuan 030032, China
2 Department of Chemistry, Hasselt University, 3590 Diepenbeek, Belgium



**ABSTRACT: Developing high-activity and low-cost catalysts is the key to eliminate the limitation of sluggish anodic oxygen evolution reaction (OER) during electrocatalytic overall water splitting. Herein, Ni–Fe/black phosphorous (BP) composites are synthesized using a simple three-electrode system, where exfoliation of bulky BP and synthesis of NiFe composites are simultaneously achieved. Under light illumination, the optimized Ni–Fe/BP composite exhibits excellent photoelectrocatalytic OER performance (e.g., the overpotential is 58 mV lower than a commercial $RuO_2$ electrocatalyst at a current density of 10 mA·cm$^{-2}$). The electron transfer on this composite is proved to follow a Ni–BP–Fe pathway. The electronic structure of this Ni–Fe/BP composite is effectively regulated, leading to optimized adsorption strength of the intermediate OH* and improved intrinsic activity for the OER. Together with active sites on the support, this Ni–Fe/BP composite possesses abundant electrochemical active sites and a bug surface area for the OER. The introduction of light further accelerates the electrocatalytic OER. This work provides a novel and facile method to synthesize high-performance metal/BP composites as well as the approaches to reveal their OER mechanisms.**

**KEYWORDS: black phosphorous; (photo-)electrocatalysis; oxygen evolution reaction**

## Contents



Received February 13, 2023; accepted March 30, 2023

E-mails: zm03030225@sxnu.edu.cn (M.Z.), jiajf@dns.sxnu.edu.cn (J.J.), nianjun.yang@uhasselt.be (N.Y.)

## 1 Introduction

Electrocatalytic water splitting has been regarded as one of the most prospective approaches to acquire clean hydrogen energy. Unfortunately, it is greatly limited by the sluggish oxygen evolution reaction (OER) occurring on the anode [1–10]. Up to now, $IrO_2$ and $RuO_2$ have been considered as the most efficient catalysts for the OER [9,11–12]. Their drawbacks are quite obvious: scarcity and high cost, refraining their widespread application. In this context, many efforts have been made to develop low-cost and earth-rich catalysts for the OER. Among various potential alternatives, Ni–Fe composites have been widely employed for the OER, originating from their unique collaborative structures [7,13–15]. However, their conductivity is too low, heavily restricting their OER catalytic activity. To overcome such a challenge, Ni–Fe composites have been frequently coupled with specific materials or loaded onto the substrates that feature high electronic mobilities. One promising substrate to load the catalysts of Ni–Fe composites is black phosphorus (BP) in that this recently emerging two-dimensional (2D) material owns inherent features (e.g., high carrier mobility, strong optical adsorption, and tunable direct band) [16–25]. To synthesize these Ni–Fe/BP hybrids, Ni–Fe and BP must be separately synthesized in the first preparation step.

Herein, we propose in this work to simultaneously produce active Ni–Fe composites and conductive BP nanosheets only by use of a home-made three-electrode system, where one single cathode and two anodes are equipped [26–30]. The application of voltage is expected to result in the exfoliation of bulky BP into BP nanosheets at the cathode and meanwhile the generation of NiFe composites at the anode. This approach is much simple than those reported protocols to Ni–Fe/BP hybrids. Moreover, the consumed energy will be reduced. Furthermore, it is known that both BP and Fe-based materials have been widely applied as the photocatalysts, due to their specific band structures [31–33]. The proposed Ni–Fe/BP hybrid is thus expected to promote the OER activity once it is illuminated.

Many reports have revealed that a typical OER electrocatalyst follows an adsorbate evolution mechanism (AEM) during the OER process. Namely it experiences a stepwise adsorption–deprotonation–coupling–desorption procedure [16]. This AEM is often interpreted using the density functional theory (DFT) method, namely to explore the influence of adsorption strength to OH* on the OER performance of an electrocatalyst.

With introduction of light irradiation, a new photoelectrocatalytic path is added. Excitation by the photon energy could generate the photoelectrons in conduction band (CB) and photogenerated carriers or holes in valence band (VB). The formation of intermediate can greatly enhance its catalytic activity by reducing the energy barrier and improving the kinetic activity. In view of this, here light irradiation is introduced in the OER, as previous work shown in superior materials such as cobaltite and hematite [34–38].

In this contribution, we report about the synthesis of the Ni–Fe/BP hybrids/composites using a simple and universal electrochemical synthesis method as well as their performance toward photoelectrocatalytic OER. Different from those theoretical tools, experimental methods have been applied to certify the AEM. The investigation of OH* adsorption on the catalyst has been probed by use of a methanol oxidation reaction (MOR) under the identified operating conditions for the OER. The OER performance of these Ni–Fe/BP composites has been also compared with the commercially available OER catalyst — noble $RuO_2$ in terms of its electrochemical active surface area, adsorption behavior, and photoelectric effect.

## 2 Experimental

### 2.1 Chemicals and materials

Tetrabutylammonium tetrafluoroborate ($TBABF_4$, 98%, solid) and propylene carbonate (PC, 99.9%, powder) were bought from Aladdin. Nickel wire and iron wire were purchased from Runde Metal Materials Company. Bulk BP was purchased from Kunming BP Technology Service Co., Ltd.

### 2.2 Preparation of Ni–Fe/BP

Nickel hydroxide, ferric oxide, and thin-layer BP were simultaneously pre-made via electrolysis at a voltage of 30 V for 2 h in a self-designed three-electrode system, where one single cathode and two anodes were equipped [26–30]. In a 0.1 $mol \cdot L^{-1}$ solution of $TBABF_4$, polished nickel and iron wires were fixed as the anode, and crushed block BP that was wrapped with a filter membrane was immobilized on the cathode. The electrolyte was

ultrasonically dispersed for 2 h and then transferred to an autoclave where a solvothermal reaction occurred at 160 °C for 12 h. After the resultant solution was washed with PC (98%) and pure ethanol for 3 times, it was dried in vacuum. The nickel hydroxide-iron oxide/BP (Ni–Fe/BP) was synthesized. The catalysts that were prepared by replacing one iron wire and one nickel wire with two nickel wires or two iron wires as the anodes are defined in this contribution as Ni/BP and Fe/BP, respectively. After the electrolysis was completed, the rest BP (after electrochemical stripping) was taken out from the cathode and put into the unreacted solution to continue the reaction. As-obtain product was defined as the BP catalyst. The applied voltage is set as 30 V to support the power source for moving large-sized $TBA^+$ cations and dissolving the iron (or nickel) wire anode; tetrabutylammonium tetrafluoroborate electrolyte and propylene carbonate solvent are used to enter into interlayer of black phosphorous for promoting the exfoliation; the solvothermal temperature of 160 °C is chosen to combine the BP NSs with metal species.

### 2.3 Characterization

Phase analysis of these catalysts was carried out by X-ray diffraction (XRD, Bruker D8 powder diffractometer with the Cu Kα radiation, $\lambda$ = 0.154 nm). The composition and oxidation states of these catalysts were examined using X-ray photoelectron spectroscopy (XPS, Thermo ESCALAB-210). Their morphologies and structures were characterized using scanning electron microscopy (SEM, Thermo, INSPECT F50) and transmission electron microscopy (TEM, JEOL, Jem 2100F).

### 2.4 Electrochemical measurements

Electrochemical tests were carried out on a CHI760E electrochemical workstation (CH Instruments, USA) using a three-electrode setup. The working electrode was prepared as follows: 5 mg of the catalyst was added into 1 mL of a mixed solvent (20 μL 5 wt.% Nafion, 290 μL $H_2O$, and 790 μL ethanol) till an ink was formed with aid of ultrasonication. On the surface of a glassy carbon electrode with a geometric area of 0.03 $cm^2$, 5 μL of this ink was casted and dried. The Hg/HgO electrode and a graphite rod were used as reference electrode and counter electrode, respectively. Throughout the paper, the Hg/HgO reference electrode was calibrated with respect to a reversible hydrogen electrode (RHE) in 1 $mol \cdot L^{-1}$ KOH using the equation of $E$/(V *vs.* RHE) = $E$/(V *vs.* Hg/HgO) + 0.059pH + 0.098 = $E$/(V *vs.* Hg/HgO) + 0.924. The electrochemical tests under light illumination were conducted using a xenon lamp. A voltage of 14 V and a corresponding current of 20 A were applied.

## 3 Results and discussion

According to our previous work [26–30,39], the application of a high working voltage (e.g., 30 V) leads to the migration of large-sized $TBA^+$ cations in solution to the cathode and further their insertion into the interlayer of bulky BP, namely the exfoliation of bulky BP into nanosheets (Fig. 1) [40]. At the same time, Ni ions or Fe ions that are generated via anodic oxidation of the electrode are solved into the electrolyte solution and then evolved as the precursors of NiFe composites. A subsequent solvothermal treatment of as-obtained results in the formation of the Ni–Fe/BP hybrids. Noticeably, our experimental results suggest the properties of used electrolytes are significantly altered under such a high voltage since it mainly determines the oxidation states of involved metal ions, which are in turn the sources of electrocatalytic activities of the Ni–Fe/BP hybrids.

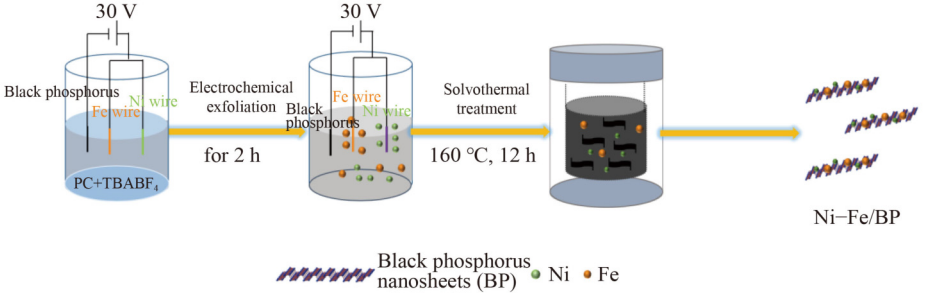


**Fig. 1** Schematic plot of electrochemically synthesizing the Ni–Fe/BP composites.

The Ni/BP, Fe/BP, Ni–Fe/BP, and BP catalysts were firstly characterized using XRD. In their XRD spectra (Fig. 2(a)), three main characteristic peaks are located at 16.9°, 34.1°, and 52.3°, which can be assigned to the (0 2 0),

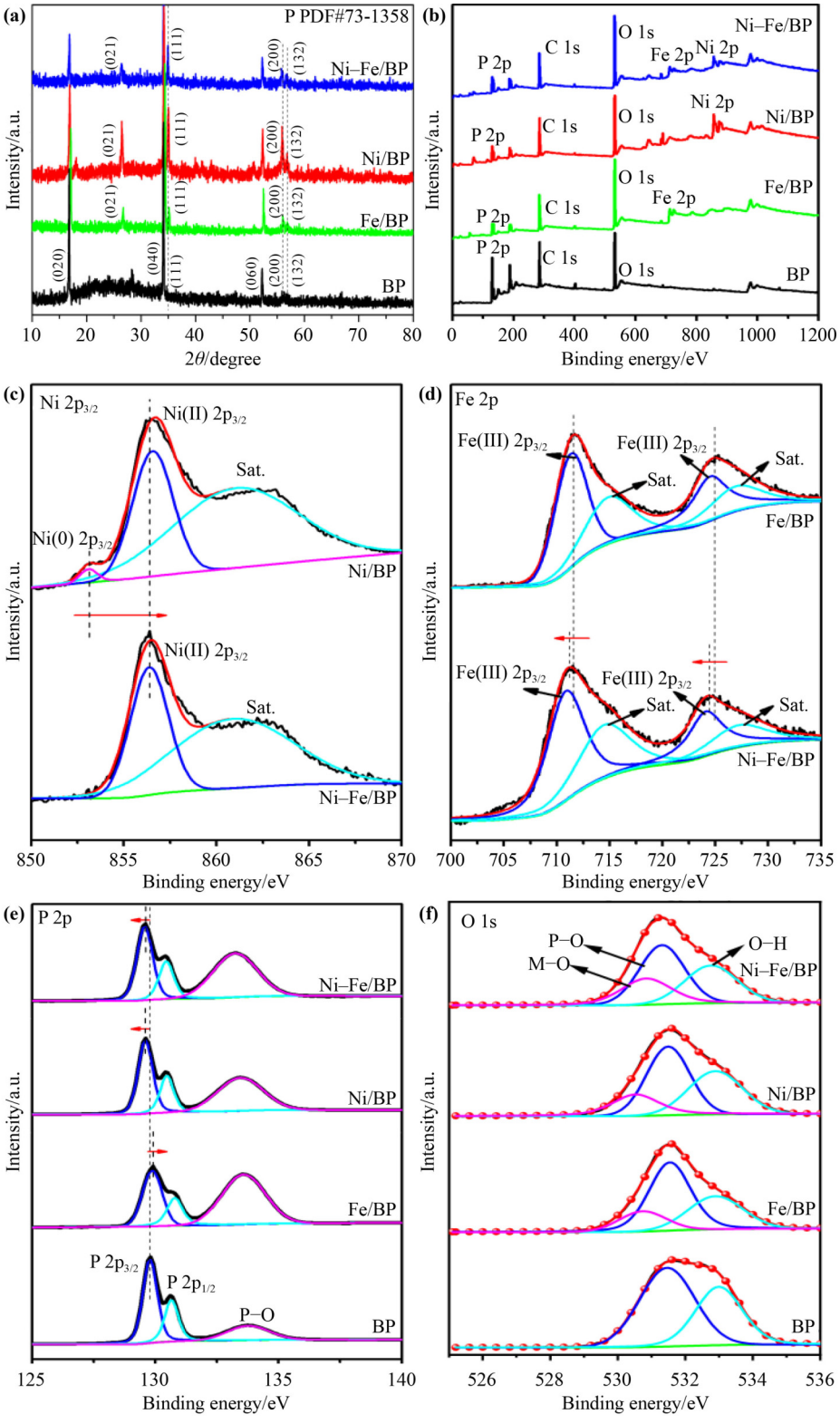


**Fig. 2** (**a**) XRD patterns and (**b**) XPS survey spectra of BP nanosheets, Ni/BP, Fe/BP, and Ni–Fe/BP catalysts. (**c**) Ni 2p XPS spectra of the Ni/BP and Ni–Fe/BP catalysts. (**d**) Fe 2p XPS spectra of the Fe/BP and Ni–Fe/BP catalysts. (**e**) P 2p and (**f**) O 1s XPS spectra of BP nanosheets, Ni/BP, Fe/BP, and Ni–Fe/BP catalysts.

(0 4 0), and (0 6 0) planes of BP, respectively (PDF #73-1358). Meanwhile, the tiny peaks at 26.4°, 35.0°, 55.8°, and 56.7° result from the (0 2 1), (1 1 1), (2 0 0), and (1 3 2) planes of BP, respectively. No obvious diffraction peaks are observed, corresponding to nickel or iron species in XRD patterns of the Ni/BP, Fe/BP, and Ni–Fe/BP catalysts. This indicates that the crystallinity of formed nickel or/and iron species over BP supporter is very low, due to their small size or mixing with amorphous structure [16].

In the XPS survey spectra of the Ni/BP, Fe/BP, and Ni–Fe/BP catalysts (Fig. 2(b)), the signals of nickel or/and iron species are noticed. In other words, nickel or/and iron species are successfully loaded on the BP nanosheets. The contents of nickel or/and iron were further calculated by use of inductively coupled plasma-optical emission spectroscopy (ICP-OES) (Table S1). The Ni content is 19.53 wt.% for the Ni/BP catalyst, while the content of Fe is 22.54 wt.% for the Fe/BP catalyst. For the Ni–Fe/BP catalyst, the contents of Ni and Fe are 12.08 and 12.68 wt.%, respectively. Meanwhile, in the Ni 2p XPS spectra (Fig. 2(c)) for the Ni/BP and Ni–Fe/BP catalysts, two main peaks are located at about 856.4 and 861.2 eV, typical for $Ni^{2+}$ species and the corresponding satellite peak, respectively. Noticeably, a new peak in the Ni 2p XPS spectrum of the Ni/BP catalyst arises at 853.0 eV, corresponding to $Ni^0$ in $Ni_xP$ [17]. However, the introduction of Fe leads to the disappearance of this peak, an indication of structure transformation of original Ni species by the added Fe species. The incorporation of Fe is supposed to promote the oxidation of $Ni^0$ to $Ni^{2+}$ species or electron transfer to Ni species. The formed $Ni^{2+}$ species on the Ni/BP catalyst is believed to be α-$Ni(OH)_2$, which can be oxidized. Such an oxidation process stems from the conversion of α-$Ni(OH)_2$ to γ-NiOOH [3]. Interestingly, this oxidation peak almost is not expected for the Ni–Fe/BP catalyst, due to the incorporation of Fe species.

In the Fe 2p XPS spectrum of the Fe/BP catalyst (Fig. 2(d)), two characteristic peaks appear at 711.4 and 724.6 eV, indicating the formation of $Fe^{3+}$ species. Compared with those of the Ni/BP catalyst, a negative shift of the binding energy (BE) by about 0.4–0.5 eV is observed for the Ni–Fe/BP catalyst. The introduction of Ni brings in the transfer of more electrons to Fe species. The P 2p XPS spectra of the BP, Ni/BP, and Fe/BP catalysts were recorded and compared (Fig. 2(e)). The P 2p peaks in the XPS spectrum of the BP catalyst obviously shift when it is incorporated with Ni (or Fe) species. The P 2p peaks in the XPS spectrum of the BP catalysts just appear at the middle between those of the Fe/BP and Ni/BP catalysts. This is because these introduced Ni (or Fe) species exhibit strong electron interactions with BP. Moreover, the peak in the O 1s XPS spectrum (Fig. 2(f)) of the BP nanosheets were deconvoluted into two peaks at 532.9 and 530.9 eV, assigned to OH and P−O groups, respectively. In addition to these two peaks, a new peak is seen in the spectra of the Ni/BP, Fe/BP, and Ni–Fe/BP catalysts, an indication of the formation of an oxygen–metal (O−M) bond. Consequently, metal oxides/oxyhydroxides are formed in these catalysts.

Combining with these XPS results, one can tell that a pathway for the Ni–Fe/BP catalyst to transfer electrons is formed: $Ni_xP$(α-$Ni(OH)_2$)–BP–$Fe_2O_3$. Namely, the electrons migrate from Ni species to Fe species along the BP bridge. The electronic structure of such a Ni–Fe/BP composite is expected to be effectively regulated. Its adsorption and electrocatalytic behavior will be finally optimized.

The morphology of these catalysts was checked using SEM. In the SEM images of the Ni/BP (Fig. S1(a)) and Fe/BP (Fig. S1(b)) catalysts, one can clearly see that small nanoparticles are distributed over the surface of BP nanosheets. After the loading of both Ni and Fe species onto the BP nanosheets (Fig. S1(c)), large nanoparticles are observed (Fig. 3(a)). The nanostructure of these Ni–Fe/BP nanoparticles was further revealed by means of TEM, high-resolution TEM (HRTEM), and scanning TEM (STEM). In their TEM image, small irregular aggregates are dispersed on lamellar BP nanosheets (Fig. 3(b)). These BP nanosheets are mainly composed of the crystal face of (0 4 0), inferred from an interplanar distance of 0.263 nm (Fig. 3(c)). In addition, the emerging lattice fringe spacings of 0.256 nm (Fig. 3(d)) and 0.252 nm (Fig. 3(e)) are noticed, well matched with the (0 0 9) plane of $Ni(OH)_2$ and the (3 1 1) plane of $Fe_2O_3$, respectively. The corresponding elemental mapping images of P (Fig. 3(g)), Ni (Fig. 3(h)), O (Fig. 3(i)), and Fe (Fig. 3(j)) reveal the uniform distribution of these elements. All these results verify the successful and uniform loading of the NiFe composites on the BP nanosheets, consistent with the results obtained from XPS analysis. The Ni–Fe/BP composites are formed inside the Ni–Fe/BP catalyst.

As-prepared catalysts were then employed as the OER

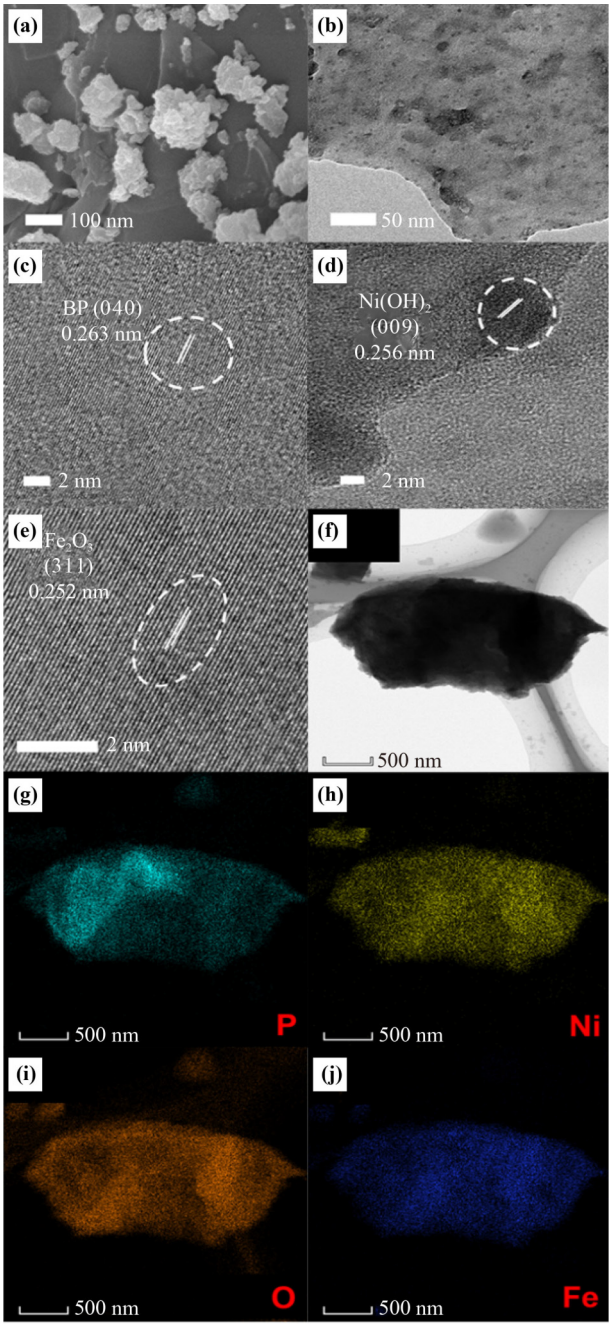


**Fig. 3** (**a**) SEM image, (**b**) TEM image, (**c**)(**d**)(**e**) HRTEM images, (**f**) HAADF-STEM image, and (**g**)(**h**)(**i**)(**j**) corresponding EDS mapping images of the Ni–Fe/BP catalyst.

photoelectrocatalysts. Their intrinsic activity toward photoelectrocatalytic OER was firstly evaluated by means of linear sweep voltammetry (LSV) (Fig. 4(a)). In some cases, light was illuminated. The corresponding overpotentials obtained at a current density of 10 $mA \cdot cm^{-2}$ (without iR-compensation) are further compared (Fig. 4(b)). Without light illumination, the overpotentials of the Ni–Fe/BP, Ni/BP, Fe/BP, and BP catalysts are 340, 351, 407, and 415 mV, respectively. The Ni–Fe/BP catalyst has the lowest overpotential, indicating the best OER catalytic activity. This is believed that both Ni/Fe species and BP nanosheets contribute to the OER catalytic activity. A synergistic effect might exist among them. Noticeably, compared with Fe/BP or BP, Ni/BP shows obviously low overpotential, attributed to superior electrocatalytic OER performance for Ni species to Fe or BP.

After the introduction of light illumination, the OER activities of all these catalysts were elevated. The overpotentials of the Ni–Fe/BP, Ni/BP, Fe/BP, and BP catalysts decrease by 57, 40, 54, and 10 mV, respectively. For the Ni–Fe/BP catalyst, its overpotential drops down to 283 mV, stemming from its excellent photocatalytic features. UV–vis diffuse reflectance spectra of these catalysts were recorded (Fig. S2). It is concluded that band gap energy ($E_g$) values of BP nanosheets and the Fe/BP catalyst are lower than those of the Ni–Fe/BP and Ni/BP catalysts, meaning superior photoresponse of BP nanoparticles and the Fe/BP catalyst to Ni–Fe/BP or Ni/BP. This photoelectric effect was further tested (Fig. S3). Once light is on, the photocurrents on the Ni–Fe/BP, Ni/BP, Fe/BP, and BP catalysts are quickly enhanced. Big photocurrents or high photocurrent densities are found for BP nanosheets and the Fe/BP catalysts. These values are much higher than those of the Ni–Fe/BP and Ni/BP catalysts. In this context, there is strong photocurrent response caused by BP nanosheets and Fe species. When the light turned off, the Ni–Fe/BP catalyst showed the slowest decrease rate of the current and required the longest time to let the current back to zero. This tendency affirms its highest separation efficiency of electrons/holes among these catalysts [31].

The intrinsic activity of these catalysts as the photoanodes was investigated by examining their turnover frequency (TOF) values (Table S1). The TOF value of the Ni–Fe/BP catalyst is 0.4699 $s^{-1}$ at 1.60 V (*vs.* RHE), higher than those of the Ni/BP (0.448 $s^{-1}$) and the Fe/BP (0.0667 $s^{-1}$) catalysts, again proving the superior catalytic ability of the Ni–Fe/BP composites or the synergistic effect between Ni and Fe components inside the Ni–Fe/BP catalyst. The corresponding Tafel slope of the Ni–Fe/BP catalyst (Fig. 4(c)) is 55.14 $mV \cdot dec^{-1}$, lower than those of the Ni/BP catalyst (72.15 $mV \cdot dec^{-1}$), the Fe/BP catalyst (109.48 $mV \cdot dec^{-1}$), and the BP nanosheets (129.76 $mV \cdot dec^{-1}$). This indicates that the rate-limiting step is changed from the chemical reaction process to the electron–proton reaction process, and the electron transfer

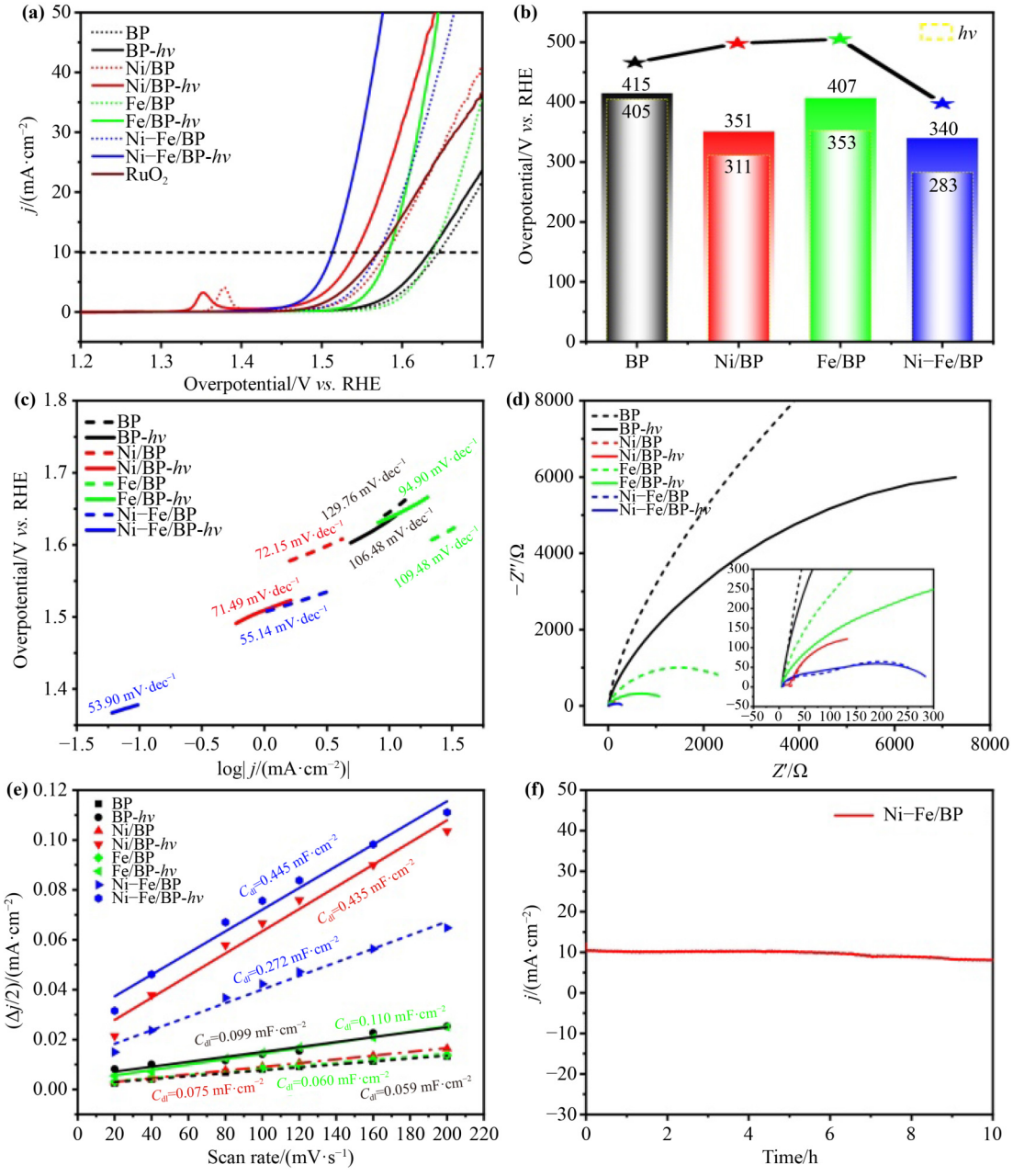


**Fig. 4** (**a**) LSV results, (**b**) overpotential comparison, (**c**) Tafel plots, (**d**) Nyquist plots, and (**e**) $C_{dl}$ values of BP nanosheets as well as the Ni–Fe/BP, Ni/BP, and Fe/BP catalysts. (**f**) Chronoamperometric curve of the Ni–Fe/BP catalyst at a constant potential of 1.57 V.

rate turns faster, which results from the composite synergy of Ni–Fe/BP. After the application of light illumination, the Tafel slopes of all catalysts are decreased. A difference value between those with and without the light illumination ($\Delta$) was defined and calculated. For the Fe/BP, BP, Ni/BP, and Ni–Fe/BP catalysts, the values of $\Delta_{Fe/BP}$, $\Delta_{BP}$, $\Delta_{Ni/BP}$, and $\Delta_{Ni–Fe/BP}$ are 14.58, 23.28, 0.66, and 1.24 mV·dec$^{-1}$, respectively. This tendency confirms again that the light illumination significantly promotes the electron transfer rates of these catalysts. Such a statement was further verified by means of electrochemical impedance spectroscopy (EIS). Since the diameters in Nyquist plots of these catalysts (Fig. 4(d)) follow a sequence of Ni–Fe/BP < Ni/BP < Fe/BP < BP.

In addition to the promoted intrinsic activity of the Ni–Fe/BP catalyst for the boosted OER, the amount of active sites on the Ni–Fe/BP catalyst is increased. This was confirmed by measuring and comparing electrochemical active surface areas (ECSAs) of used catalysts. The ECSAs can be referred to related double-layer capacitance

($C_{dl}$) (Fig. 4(e)), which are possible to be estimated from their cyclic voltammograms recorded within a non-Faradaic potential domain at different scan rates (Fig. S4). The obtained $C_{dl}$ values of these catalysts increase in the order of BP < Fe/BP < Ni/BP < Ni–Fe/BP. Clearly, the Ni–Fe/BP catalyst provides the highest amount of active sites toward the OER. The active sites of these catalysts are supposed to be further increased under light illumination, due to the generated current carriers by a photoelectric effect [41]. In addition to such excellent OER activity, this Ni–Fe/BP catalyst shows high stability, inferred from a long-term test for 10 h by use of chronoamperometry (Fig. 4(f)).

Adsorption of $OH^-$ and subsequently the formation of OH* are the first two steps involved in a complicated OER process. The bonding strength of absorbed OH* on a studied catalyst is thus the most important parameter, which decides the formation of oxygen intermediates (e.g., O* and OOH*) and eventually the whole performance of the OER. In other words, design and synthesis of an OER catalyst with a favorable bonding strength of OH* is very important. Since OH* species are electrophiles and can be detected by nucleophiles such as methanol molecules, the adsorption strength of OH* is possible to be detected using the MOR when the identified working conditions for the OER is applied [42]. The degree of surface OH* coverage or the OH* adsorption ability can be reflected with the current difference between the LSV results of the MOR and the OER, which are shown in filled areas (Fig. 5). The current difference is reduced, following the tendency of $S_{Ni–Fe/BP}$ (2.022) > $S_{Ni/BP}$ (0.380) > $S_{BP}$ (0.152) > $S_{Fe/BP}$ (0.024). Consequently, the adsorption strength toward OH* on these catalysts varies in the trend of Ni–Fe/BP > Ni/BP > BP > Fe/BP. Noticeably, the introduction of Ni to the BP nanosheets strengthens the OH* adsorption. In contrast, the incorporation of Fe to the BP nanosheets weakens the OH* adsorption. Among the studied catalysts, the Ni–Fe/BP catalyst displays the strongest OH* adsorption. Namely, the improved OER catalytic performance of the Ni–Fe/BP catalyst results from its favorable adsorption of OH* species.

As is discussed above, this obtained Ni–Fe/BP catalyst exhibits superior photoelectrocatalytic performance towards OER. The improved OER performance is assumed to result from the composition effect reflected in

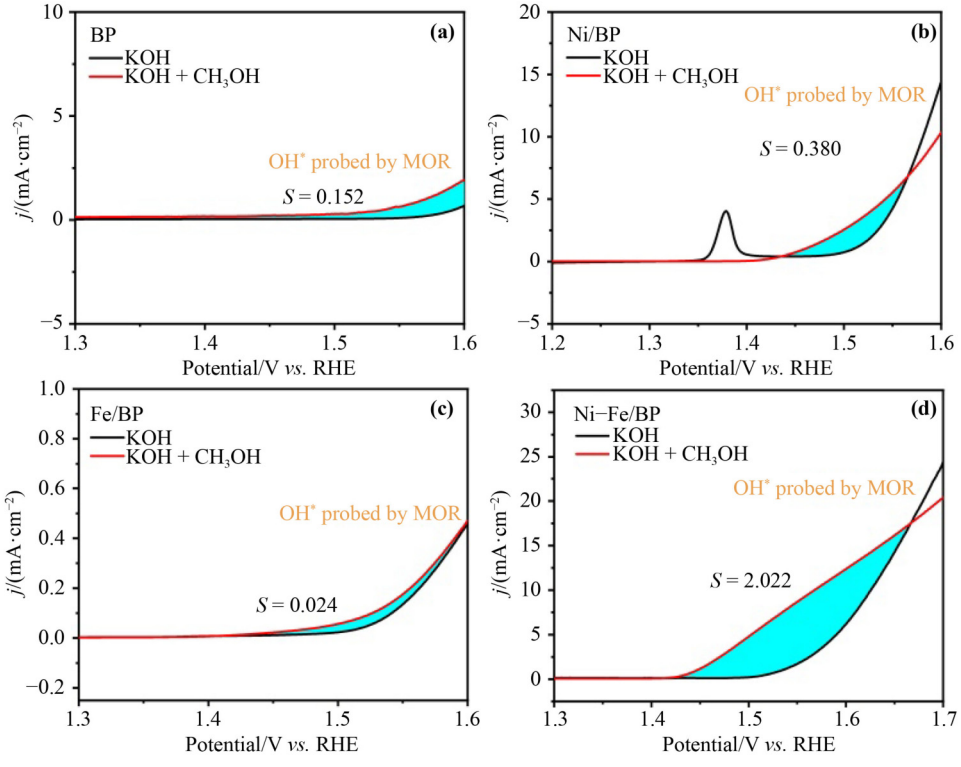


**Fig. 5** LSVs of oxygen intermediates during the MOR on (**a**) BP nanosheets as well as (**b**) Fe/BP, (**c**) Ni/BP, and (**d**) Ni–Fe/BP catalysts in 1 mol·$L^{-1}$ KOH (black) and 1 mol·$L^{-1}$ KOH + $CH_3OH$ (purple) at a scan rate of 50 mV·$s^{-1}$. These filled areas are the current difference that is caused by the MOR.

three aspects (Fig. 6). Firstly, the formed Ni–BP–Fe electron-transfer pathway inside this catalyst effectively regulates its intrinsic structure, which in turn enlarges adsorption strength of the intermediate OH* species. Secondly, three composites, namely Ni, Fe, and BP contribute together to the ECSAs, or provide abundant active sites for the OER. Thanks to *d* orbitals inside Ni and Fe species, the NiFe composites offer intrinsic active sites for the OER [43]. Meanwhile, abundant edge sites on the BP nanosheets serve active sites for the $O_2$ evolution [44]. Thirdly, the introduction of light leads to a photocurrent effect, where the Ni–Fe/BP composite is optimized, the number of active sites is increased, and eventually the original electrocatalytic OER activity is enhanced [20,45].

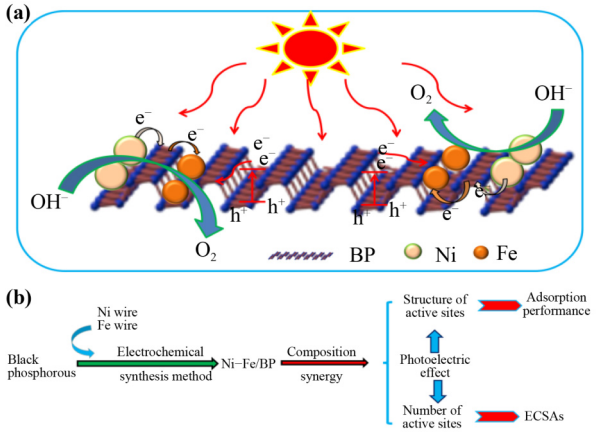


**Fig. 6** (**a**) Schematic illustration of as-proposed reaction mechanism. (**b**) Composition effect of the Ni–Fe/BP catalyst for the promoted OER.

## 4 Conclusions

In summary, a Ni–Fe/BP composite has been designed and electrochemically synthesized using a simple three-electrode electrolysis system where a single cathode and two anodes are equipped. The advantage of this approach is to simultaneously achieve exfoliation of bulky black phosphorus into nanosheets at the cathode into nanosheets and the synthesis of Ni–Fe composites evolved from the anode. This method is facile and universal for electrochemical synthesis of other BP based catalysts for different catalytic reactions such as OER, hydrogen evolution reaction, $CO_2$ reduction, nitrogen fixation/nitrite reduction, and chloride/hydrogen peroxide production. More importantly, these Ni–Fe/BP catalysts show excellent OER activity under dark conditions and light illumination. A Ni–BP–Fe electron-transfer pathway inside these Ni–Fe/BP catalysts and their superior photoelectric effects are the sources of such superior OER performance. The synergetic effect between individual components of these Ni–Fe/BP catalysts is also proposed and proved as demonstrated using their ECSAs and adsorption strength of OH* species. Consequently, this study paves a new way to design, synthesize and employ new composted catalysts for different photoelectrocatalytic applications.

**Disclosure of potential conflicts of interests** The authors declare that they have no known competing financial interests or personal relationships that could have appeared to influence the work reported in this paper.

**Acknowledgements** This work was financially supported by the National Natural Science Foundation of China (Grant No. 21571119), the Applied Basic Research Project of Shanxi Province (Grant Nos. 201901D211393 and 201901D211398), the Natural Science Foundation of Shanxi Province (Grant No. 20210302124473), the Scientific and Technological Innovation Programs of Higher Education Institution in Shanxi (Grant No. 2019L0466), the Graduate Education Innovation Project of Shanxi Province (Grant No. 2021Y480), the China postdoctoral Science Foundation (Grant No. 2021M691366), the Graduate Education Innovation Project of Shanxi Normal University (Grant No. 2021XSY038), and the 1331 Engineering of Shanxi Province.

**Electronic supplementary information** Supplementary materials can be found in the online version at https://doi.org/10.1007/s11706-023-0646-8, which include Figs. S1–S4 and Table S1 revealing results from SEM, CV, and transient photocurrent test.

## References

[1] Francàs L, Corby S, Selim S, et al. Spectroelectrochemical study of water oxidation on nickel and iron oxyhydroxide electrocatalysts. Nature Communications, 2019, 10(1): 5208

[2] Suen N T, Hung S F, Quan Q, et al. Electrocatalysis for the oxygen evolution reaction: recent development and future perspectives. Chemical Society Reviews, 2017, 46(2): 337–365

[3] Dai L, Chen Z N, Li L, et al. Ultrathin $Ni^0$-embedded $Ni(OH)_2$ heterostructured nanosheets with enhanced electrochemical overall water splitting. Advanced Materials, 2020, 32(8): 1906915

[4] Zhu K, Zhu X, Yang W. Application of *in situ* techniques for the characterization of NiFe-based oxygen evolution reaction (OER) electrocatalysts. Angewandte Chemie International Edition, 2019, 58(5): 1252–1265

[5] Maruthapandian V, Kumaraguru S, Mohan S, et al. An insight on the electrocatalytic mechanistic study of pristine Ni MOF (BTC)

in alkaline medium for enhanced OER and UOR. ChemElectroChem, 2018, 5(19): 2795–2807

[6] Diaz-Morales O, Ferrus-Suspedra D, Koper M T M. The importance of nickel oxyhydroxide deprotonation on its activity towards electrochemical water oxidation. Chemical Science, 2016, 7(4): 2639–2645

[7] Trotochaud L, Young S L, Ranney J K, et al. Nickel–iron oxyhydroxide oxygen-evolution electrocatalysts: the role of intentional and incidental iron incorporation. Journal of the American Chemical Society, 2014, 136(18): 6744–6753

[8] Trześniewski B J, Diaz-Morales O, Vermaas D A, et al. *In situ* observation of active oxygen species in Fe-containing Ni-based oxygen evolution catalysts: the effect of pH on electrochemical activity. Journal of the American Chemical Society, 2015, 137(48): 15112–15121

[9] Xue Z, Liu K, Liu Q, et al. Missing-linker metal-organic frameworks for oxygen evolution reaction. Nature Communications, 2019, 10(1): 5048

[10] Tuček J, Holá K, Bourlinos A B, et al. Room temperature organic magnets derived from $sp^3$ functionalized graphene. Nature Communications, 2017, 8(1): 14525

[11] Shi Q, Zhu C, Du D, et al. Robust noble metal-based electrocatalysts for oxygen evolution reaction. Chemical Society Reviews, 2019, 48(12): 3181–3192

[12] Zhou Y, Sun S, Wei C, et al. Significance of engineering the octahedral units to promote the oxygen evolution reaction of spinel oxides. Advanced Materials, 2019, 31(41): 1902509

[13] Zeng L, Yang L, Lu J, et al. One-step synthesis of Fe–Ni hydroxide nanosheets derived from bimetallic foam for efficient electrocatalytic oxygen evolution and overall water splitting. Chinese Chemical Letters, 2018, 29(12): 1875–1878

[14] Chen G, Zhu Y, Chen H M, et al. An amorphous nickel–iron-based electrocatalyst with unusual local structures for ultrafast oxygen evolution reaction. Advanced Materials, 2019, 31(28): 1900883

[15] Kuai C, Zhang Y, Wu D, et al. Fully oxidized Ni–Fe layered double hydroxide with 100% exposed active sites for catalyzing oxygen evolution reaction. ACS Catalysis, 2019, 9(7): 6027–6032

[16] Chen H, Chen J, Ning P, et al. 2D heterostructure of amorphous CoFeB coating black phosphorus nanosheets with optimal oxygen intermediate absorption for improved electrocatalytic water oxidation. ACS Nano, 2021, 15(7): 12418–12428

[17] Wang J, Liu D, Huang H, et al. In-plane black phosphorus/dicobalt phosphide heterostructure for efficient electrocatalysis. Angewandte Chemie International Edition, 2018, 57(10): 2600–2604

[18] Shi F, Geng Z, Huang K, et al. Cobalt nanoparticles/black phosphorus nanosheets: an efficient catalyst for electrochemical oxygen evolution. Advanced Science, 2018, 5(8): 1800575

[19] Li X, Xiao L, Zhou L, et al. Adaptive bifunctional electrocatalyst of amorphous CoFe oxide@2D black phosphorus for overall water splitting. Angewandte Chemie International Edition, 2020, 59(47): 21106–21113

[20] Bai L, Wang X, Tang S, et al. Black phosphorus/platinum heterostructure: a highly efficient photocatalyst for solar-driven chemical reactions. Advanced Materials, 2018, 30(40): 1803641

[21] Wang N, Mao N, Wang Z, et al. Electrochemical delamination of ultralarge few-layer black phosphorus with a hydrogen-free intercalation mechanism. Advanced Materials, 2021, 33(1): 2005815

[22] Wang X, Raghupathy R K M, Querebillo C J, et al. Interfacial covalent bonds regulated electron-deficient 2D black phosphorus for electrocatalytic oxygen reactions. Advanced Materials, 2021, 33(20): 2008752

[23] Liang T, Liu Y, Cheng Y, et al. Scalable synthesis of a $MoS_2$/black phosphorus heterostructure for pH-universal hydrogen evolution catalysis. ChemCatChem, 2020, 12(10): 2840–2848

[24] Zou B, Qiu S, Ren X, et al. Combination of black phosphorus nanosheets and MCNTs via phosphoruscarbon bonds for reducing the flammability of air stable epoxy resin nanocomposites. Journal of Hazardous Materials, 2020, 383: 121069

[25] Zhang Y, Wang L, Xu H, et al. 3D chemical cross-linking structure of black phosphorus@CNTs hybrid as a promising anode material for lithium ion batteries. Advanced Functional Materials, 2020, 30(12): 1909372

[26] Xiao H, Du X, Zhao M, et al. Structural dependence of electrosynthesized cobalt phosphide/black phosphorus pre-catalyst for oxygen evolution in alkaline media. Nanoscale, 2021, 13(15): 7381–7388

[27] Xiao H, Zhang J, Zhao M, et al. Electric field-assisted synthesis of Pt, carbon quantum dots-coloaded graphene hybrid for hydrogen evolution reaction. Journal of Power Sources, 2020, 451: 227770

[28] Xiao H, Xue S, Zhang J, et al. Facile electrolytic synthesis of Pt and carbon quantum dots coloaded multiwall carbon nanotube as highly efficient electrocatalyst for hydrogen evolution and ethanol oxidation. Chemical Engineering Journal, 2021, 408: 127271

[29] Zhao M, Xue S, Xiao H, et al. Facile *in-situ* electrochemical fabrication of highly efficient nickel hydroxide–iron hydroxide/graphene hybrid for oxygen evolution reaction. International Journal of Hydrogen Energy, 2022, 47(25): 12547–12558

[30] Xiao H, Li B, Zhao M, et al. Electrosynthesized $CuO_x$/graphene by a four-electrode electrolysis system for the oxygen reduction

reaction to hydrogen peroxide. Chemical Communications, 2021, 57(34): 4118–4121

[31] Li S, Zhang Y, Huang H. Black phosphorus-based heterostructures for photocatalysis and photoelectrochemical water splitting. Journal of Energy Chemistry, 2022, 67: 745–779

[32] Liardet L, Katz J E, Luo J, et al. An ultrathin cobalt–iron oxide catalyst for water oxidation on nanostructured hematite photoanodes. Journal of Materials Chemistry A: Materials for Energy and Sustainability, 2019, 7(11): 6012–6020

[33] Asif S A, Khan S B, Asiri A M. Efficient solar photocatalyst based on cobalt oxide/iron oxide composite nanofibers for the detoxification of organic pollutants. Nanoscale Research Letters, 2014, 9(1): 510

[34] Tomon C, Sarawutanukul S, Phattharasupakun N, et al. Insight into photoelectrocatalytic mechanisms of bifunctional cobaltite hollow-nanofibers towards oxygen evolution and oxygen reduction reactions for high-energy zinc–air batteries. Electrochimica Acta, 2021, 392: 139022

[35] Xu R, Zhu D, Du K, et al. Role of surface wettability in photoelectrocatalytic oxygen evolution reactions. Materials Today Energy, 2022, 25: 100961

[36] Athar M, Fiaz M, Farid M A, et al. Iron and manganese codoped cobalt tungstates $Co_{1-(x+y)}Fe_xMn_yWO_4$ as efficient photoelectrocatalysts for oxygen evolution reaction. ACS Omega, 2021, 6(11): 7334–7341

[37] Li L, Xiao S, Li R, et al. Nanotube array-like $WO_3$ photoanode with dual-layer oxygen-evolution cocatalysts for photoelectrocatalytic overall water splitting. ACS Applied Energy Materials, 2018, 1(12): 6871–6880

[38] Zhang H, Li P, Zhou H, et al. Unravelling the synergy of oxygen vacancies and gold nanostars in hematite for the electrochemical and photoelectrochemical oxygen evolution reaction. Nano Energy, 2022, 94: 106968

[39] Zhao M, Cheng X, Xiao H, et al. Cobalt–iron oxide/black phosphorus nanosheet heterostructure: electrosynthesis and performance of (photo-)electrocatalytic oxygen evolution. Nano Resaerch, 2023, in press

[40] Liu D, Wang J, Lu J, et al. Direct synthesis of metal-doped phosphorene with enhanced electrocatalytic hydrogen evolution. Small Methods, 2019, 3(7): 1900083

[41] Zhang Y, Wang Y, Jiang H, et al. Multifunctional nickel sulfide nanosheet arrays for solar-intensified oxygen evolution reaction. Small, 2020, 16(33): 2002550

[42] Tao H B, Xu Y, Huang X, et al. A general method to probe oxygen evolution intermediates at operating conditions. Joule, 2019, 3(6): 1498–1509

[43] Friebel D, Louie M W, Bajdich M, et al. Identification of highly active Fe sites in (Ni,Fe)OOH for electrocatalytic water splitting. Journal of the American Chemical Society, 2015, 137(3): 1305–1313

[44] Jiang Q, Xu L, Chen N, et al. Facile synthesis of black phosphorus: an efficient electrocatalyst for the oxygen evolving reaction. Angewandte Chemie International Edition, 2016, 55(44): 13849–13853

[45] Han X, Yu Y, Huang Y, et al. Photogenerated carriers boost water splitting activity over transition-metal/semiconducting metal oxide bifunctional electrocatalysts. ACS Catalysis, 2017, 7(10): 6464–6470